Solar Physics (2006) 233: 331–372
DOI: 10.1007/s11207-006-2058-1

CALIBRATION OF THE SOHO/LASCO C3 WHITE LIGHT CORONAGRAPH

J. S. MORRILL, C. M. KORENDYKE, G. E. BRUECKNER†, F. GIOVANE, R. A. HOWARD, M. KOOMEN, D. MOSES, S. P. PLUNKETT, and A. VOURLIDAS
Naval Research Laboratory, Code 7660, 4555 Overlook Avenue SW, Washington, DC 20375, U.S.A.
(e-mails: morrill@shogunnrl.navy.mil, clarence.korendyke@nrl.navy.mil, russ.howard@nrl.navy.mil, frank.giovane@nrl.navy.mil, dan.moses@nrl.navy.mil, simon.plunkett@nrl.navy.mil, angelos.vourlidas@nrl.navy.mil)

E. ESFANDIARI, N. RICH and D. WANG
Interferometrics, 14120 Parke Long Court, Suite 103, Chantilly, VA 20151, U.S.A.
(e-mails: ed.esfandiari@nrl.navy.mil, nathan.rich@nrl.navy.mil, dennis.wang@nrl.navy.mil)

A. F. THERNISIEN
Universities Space Research Association, 1101 17th Street NW, Suite 1004, Washington, DC 20036, U.S.A.
(e-mail: arnaud.thernisien@nrl.navy.mil)

P. LAMY and A. LLEBARIA
Laboratoire d'Astronomie Spatiale, F13376 Marseille, Cedex 12, France
(e-mails: phillippe.lamy@oamp.fr, antione.llebaria@oamp.fr)

D. BIESECKER
NOAA, Space Environment Center, 325 Broadway, Boulder, CO 80305, U.S.A.
(e-mail: doug.biesecker@noaa.gov)

D. MICHELS
The Catholic University of America, 620 Michigan Avenue NE, Washington, DC 20064, U.S.A.
(e-mail: don.michels@nrl.navy.mil)

Q. GONG
Swales Aerospace, 5050 Powder MIll Rd, Beltsville, MD 20705, U.S.A
(e-mail: qgong@swales.com)

and

M. ANDREWS
SRI International, 333 Ravenswood Ave., Menlo Park, CA 94025, U.S.A.
(e-mail: mike.andrews@sri.com)

(Received 4 March 2005; accepted 15 September 2005)

Abstract. We present a detailed review of the calibration of the LASCO C3 coronagraph on the SOHO satellite. Most of the calibration has been in place since early in the mission and has been utilized to varying degrees as required by specific analysis efforts. However, using observational data from the nearly decade-long database of LASCO images, we have re-evaluated and improved many aspects of the calibration. This includes the photometric calibration, vignetting function, geometric distortion, stray light, and exposure and observation times. Using this comprehensive set of corrections

†Deceased

we have generated and made available a set of calibrated coronal images along with a set of periodic background images to ease the accessibility and use of the LASCO database.

1. Introduction

In this paper, we present a comprehensive review of the LASCO C3 calibration. For the most part this calibration has been in place since launch. During the course of the SOHO mission further information, much of it derived from star observations, has allowed us to refine the details of this calibration. As a result, corrections to the photometric calibrations, the vignetting function, geometric distortion effects, stray light, and exposure and observation times have all been optimized. Using these recent refinements we have generated a Level-1 data set so that a majority of the C3 data set is available without need of further correction.

A broad definition of calibration is the conversion of instrumental observations from engineering units to scientific units. The corrections that must be applied vary with the instrument but often this is a vital step in the derivation of new knowledge from scientific observations. Indeed, the quality of such scientific conclusions is generally limited by the quality of the calibration applied to the basic observations. This problem is especially unique for satellite based instruments where post-launch calibration may be difficult and the observer often has fewer controls over the instrument than before launch. Care must be taken so that adequate flexibility and resources are available to ensure calibration quality both before launch and over the extended period associated with space missions.

For the LASCO C3 coronagraph, the pre-flight calibration was performed at the Naval Research Laboratory (NRL) and has proved adequate to support the many scientific analysis that have used LASCO data. It is important to note that different studies require the application of different instrumental corrections. For example, determination of CME velocities and acceleration do require corrections for geometric distortion but do not require photometric calibration. On the other hand, photometric calibrations are essential to studies that examine CME mass and energetics. The application of the relevant calibrations has been done at the discretion of the user and with advice and support from LASCO team members. During the course of the SOHO mission as the quantity of data has grown it has become possible to make improvements to the pre-flight calibration. In this paper, we present a comprehensive review of pre-flight and in-flight calibrations. This does not include polarization which is the subject of a separate paper currently in preparation. Since C3 observations have generally been made without the polarizer filters the following discussion applies to most of the C3 data set ($\sim$93%).

Although we have re-evaluated all aspects of the pre-flight calibration a number of the calibrations have been re-examined in detail. These include the vignetting function, the geometric distortion, and correction of the reported exposure time. In addition, a detailed re-evaluation of the photometric sensitivity of the various

C3 filters has been done for the period from mid-1996 through part of 2004. For the clear filter, this reevaluation has improved the photometric calibration to the point where a slight drift in the instrument response of ∼3% is evident over this 8 year period. This has allowed the determination of a time-dependent photometric calibration for the majority of the C3 observations (the clear filter observations are ∼80% of the current data set).

In the sections that follow, pre-flight calibrations will be discussed briefly with the main focus being on the in-flight efforts when they supersede the pre-flight results. The paper is organized so that each component of the calibration is discussed in a separate section and Sections 3–9 conclude with a summary. A basic description of the C3 coronagraph is presented in Section 2. The characteristics of the flight CCD are discussed in Section 3 and these are used in Section 4 which discusses C3 photometry. Sections 5 and 6 discuss the vignetting and geometric distortion, respectively. Sections 7 and 8 present the corrections to the absolute time, Sun-center location, spacecraft orientation and image exposure time corrections. Section 9 examines stray light issues while Sections 10 and 11 address the generation of background coronal images and Level-1 data processing. A discussion of the polarization calibration appears in a separate paper (Moran, Davila, Morrill *et al.*, in press).

Using the corrections presented in this paper we have generated a comprehensive calibrated data set. This data set covers all C3 color filter observations and all images have been processed as discussed in Section 11 on the Level-1 processing. Figure 1 shows a corrected coronal image with a background image subtracted. Information on how to access the C3 Level-1 data set can be found on the LASCO web site, *http://lasco-www.nrl.navy.mil/*.

2. Description of the LASCO C3 Coronagraph

In this section, we discuss the optical layout of the C3 coronagraph, the LASCO CCD camera and instrument electronics, and the telemetry, image compression and LASCO data levels.

2.1. Optical layout

The coronagraph, invented in the 1930s (Lyot, 1930), provides a view of the solar corona without a total solar eclipse. Lyot analyzed the sources of stray light generated by a telescope and developed solutions to greatly reduce their impact. Modifications to this internally occulted coronagraph concept (Evans, 1948) included putting an occulting disk in front of the objective lens. Apodizing systems were added (Purcell and Koomen, 1962; Newkirk and Bohlin, 1963) that further improved the stray light rejection. Purcell and Koomen used a serrated occulting disk, whereas Newkirk and Bohlin used a triple disk system. Both have been used

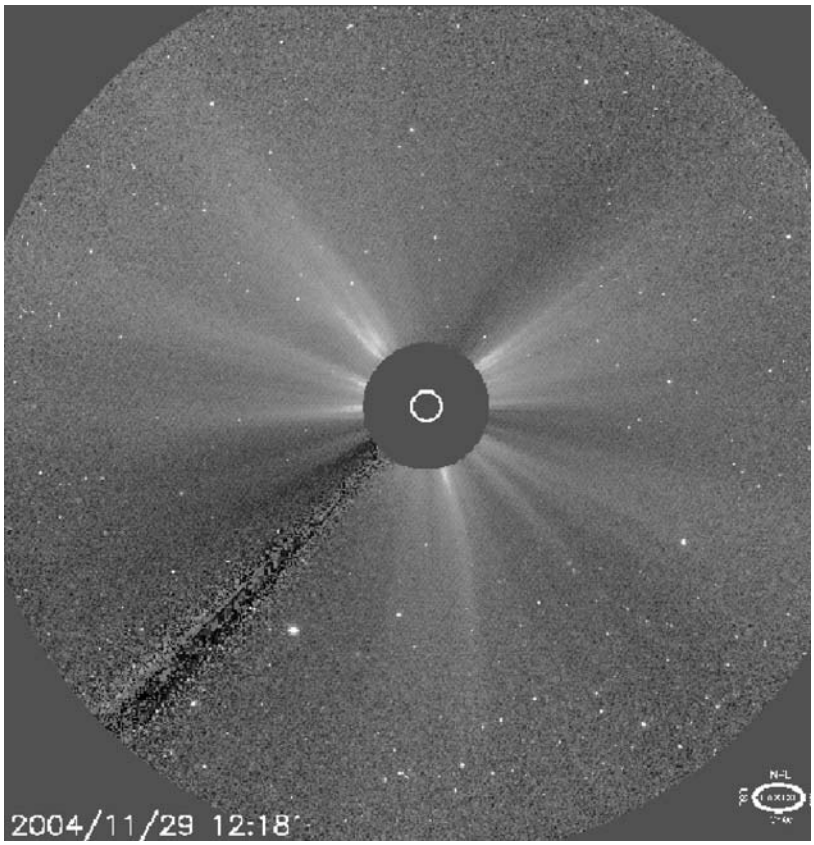

Figure 1. Corrected coronal image.

in space, but the triple disk external occulting disk system was used by the C3 coronagraph.

An externally occulted coronagraph is a telescope with an occulting disk that blocks light from the solar disk from striking the objective lens, thereby reducing stray sunlight to a level that the Sun's corona can be observed. The C3 coronagraph is one of a long line of instruments that have studied the solar corona from space. Tousey (1965) first flew an externally occulted coronagraph on a sounding rocket in 1963, which was followed by more rocket as well as balloon flights during the 1960s to develop the concept. Since then, several externally occulted coronagraphs have been flown on satellites for long-term continuous coronal observations: OSO-7 (1971–1974) (Koomen *et al.*, 1975), Skylab (1973–1974) (MacQueen *et al.*, 1974), P78-1 (1979–1985) (Koomen *et al.*, 1975), the Solar Maximum Mission (1980–1989) (MacQueen *et al.*, 1980) and the Spartan 201 coronagraph which was flown on shuttle sortie missions in 1993, 1994, 1995, and 1998. These coronagraphs brought improved spatial resolution, time resolution, and mission duration, but were confined to observing the corona over a limited range of elongation.

The LASCO field of view extends the range of these observations from 1.1 to 30 $R_{\rm Sun}$. Over this range, the K coronal brightness varies by ~5 orders of magnitude. To recover this extended range of brightness, the LASCO field-of-view (FOV) is divided into three concentric annular regions, covered by three independent optical systems, called C1, C2 and C3. This paper focuses on the C3 coronagraph that covers the outer portion of the FOV, which actually extends from 3.8 to 30 $R_{\rm Sun}$ (32 $R_{\rm Sun}$ in the corners of the FOV). The outer field limit of C2 is at 7 $R_{\rm Sun}$, giving ~3 $R_{\rm Sun}$ overlap between C2 and C3.

The externally occulted nature of C3 gives rise to a basic limitation. The limited distance between the external occulting disk and the objective lens requires an over-occulting of the solar limb. Depending on the desired outer limit, more or less over-occulting is necessary to achieve the required stray light level. The spatial resolution at the inner edge is poor, because most of the objective lens is shadowed by the external occulter, which results in a very small effective apertures at the inner edge of the field-of-view. Actually the shape of the aperture is a line which is small in the radial direction but larger in the azimuthal direction. In addition, because of size limitations on the instrument length, the objective lens aperture usually cannot exceed a few centimeters. A detailed discussion of the LASCO coronagraph optics in presented elsewhere (Brueckner *et al.*, 1995). The optical layout for C3 is shown in Figure 2.

Several design features are used in stray light suppression in addition to those suggested by Lyot. These include a serrated front aperture (A0), a field stop at the O1 objective lens image plane, a superpolished objective lens, an aperture at the image plane of the A0, a small opaque Lyot spot, and baffles located so that optical elements view only the rear surfaces of baffles, or shadowed walls. After these efforts, stray light in the system is measured to be on the order of 10^{-12} $B_{\rm Sun}$, where $B_{\rm Sun}$ is the disk average solar brightness. Because of the relatively short distance between the external occulter D1 and the entrance aperture A1, the coronal image is strongly vignetted near the center of the FOV. A compensating factor is that the brightness range of the corona at the focal plane is reduced, so that the entire coronal image can be well recorded with a single exposure. The corona becomes un-vignetted beyond ~10 $R_{\rm Sun}$.

The shutter, filter, and polarizer wheels shown in Figure 2 are between the relay lens and CCD camera. As an aid to separation of F (dust) from K (electron) coronal light, C3 has broadband color filters and polarizers for polarization analysis, and a moderately narrow (2 nm) Hα filter. The filter wheel and polarizer wheels each have five positions. The filter wheel contains the blue, orange, deep red, infrared filters, and broadband clear filters. The polarizer wheel contains three polarizers at 0°, +60°, and −60°, an Hα filter, and a clear glass position. The five color filters are used with the clear glass polarizer wheel position or one of the three polarizers.

An internal incandescent calibration lamp is located behind the shutter. When powered, light from the lamp is reflected diffusely from the rear of the shutter blade, which had been roughened, passes through a filter and a polarizer, and then

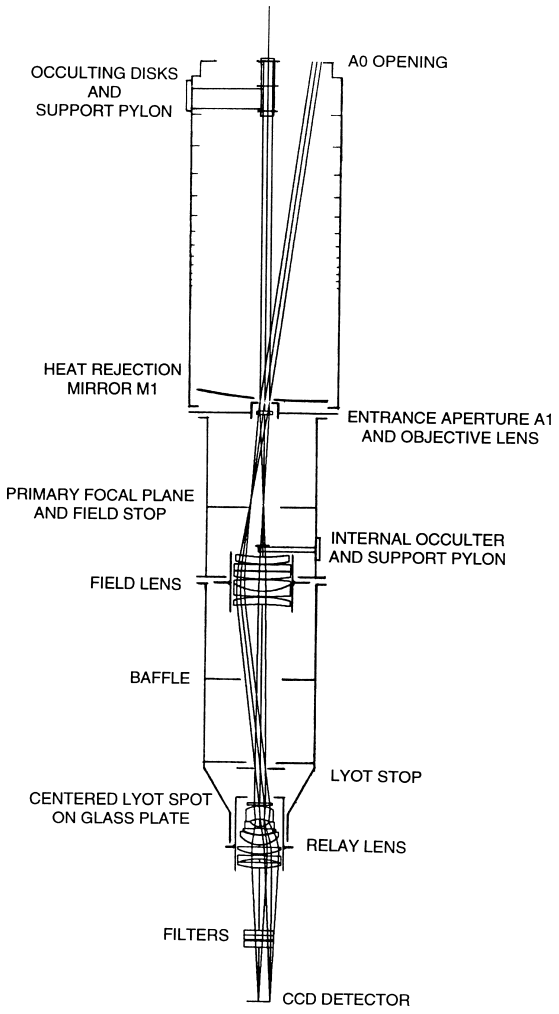

Figure 2. Optical layout of C3 coronagraph.

illuminates the CCD. Also, the signal level of the CCD detector can be monitored when the front door is closed and the shutter remains open. In this case, the coronagraph sees the rear of a small, Sun-illuminated diffuser set in the door. This patch is out of focus at the CCD, but since it is only illuminated by the highly attenuated Sun, it provides a known level of solar disk illumination.

2.2. LASCO CCD CAMERA AND ELECTRONICS BOX

The LASCO Electronics Box (LEB) supports three CCD camera/data channels for the three LASCO telescopes and one for the EIT and a channel to control the

Fabry-Perot interferometer on the C1 telescope. The camera electronics contain all of the functions required to operate the Tektronix (now SiTE) 1024 × 1024 CCDs with only high-level commands from the LEB being required. Clock-driver, pre-amplifier, and conditioning circuits for the CCDs are part of the camera units, and are contained on the plug-in camera modules. The CCD contains four readout ports with separate on-chip amplifiers. The two serial transfer registers, at either end of the CCD array, contain 20 extra pixels between the edge of the array and the readout ports at both ends. These 20 extra pixels are used to determine a number of electrical properties of the CCD. While the capability exist to change CCD readout port, in practice we have not changed the port after the initial calibration and checkout period in early 1996.

The camera control is basically identical in all four channels. The LEB contains a block-redundant CPU/power converter/memory subsystem and either processor subsystem can receive the image data from any of the four cameras. This provides considerable flexibility and redundancy. An operational restriction is that only one camera can be read out or commanded at a time. A more detailed discussion of the LEB is presented elsewhere (Brueckner *et al.*, 1995).

2.3. Telemetry modes, image compression, and levels of LASCO data

There are several telemetry submodes used in normal operations, depending on whether all SOHO instruments or a subset of instruments are operating at any time. The submode definitions have changed several times since launch. Table I shows the LASCO/EIT telemetry allocation in each of the current five submodes, and in the four submodes that were used at the time of launch. The nominal LASCO/EIT telemetry rate (submode 1) from launch in December 1995 to February 1997 was 5.2

TABLE I

Telemetry rate (kbits per second) for LASCO/EIT in each operating submode.

Submodes	1[a]	2[d]	3[d]	4[d]	5[b]	6[c,e]
Launch	5.3	26.7	5.3	5.3	–	–
Present	–	26.7	5.3	5.3	7.9	15.8

[a]Submode 1 was the nominal telemetry submode in launch configuration, and was not used after February 1997.
[b]Submode 5 was added in February 1997, and replaced Submode 1 as the nominal operating telemetry submode.
[c]Submode 1 was patched in February 1997 to give all SUMER telemetry to LASCO/EIT, and was renamed as Submode 6.
[d]CDS or SUMER High rate with LASCO unaffected.
[e]Extra rate.

kbits per second (kbps). This allocation also applies in those submodes where the CDS or SUMER instruments are operating with an increased telemetry allocation (submodes 3 and 4, respectively). The LASCO/EIT high rate submode (submode 2), with an allocation of 26.7 kbps, was used on rare occasions when both the SUMER and CDS instruments were operating in a greatly reduced operating mode and each transferred 10 kbps of their telemetry to LASCO/EIT.

New telemetry submodes were added between February and September 1997. The nominal telemetry allocation for LASCO/EIT was increased to 7.9 kbps (submode 5), and a new submode (submode 6) was created in which LASCO/EIT receives all the SUMER telemetry at times when that instrument is not operating. The LASCO/EIT allocation in submode 6 is 15.8 kbps. Except for brief periods, including the 3 month mission interruption and subsequent spacecraft recovery in 1998, the telemetry submode definitions have remained unchanged since September 1997. At the time of writing, SUMER only observes for brief periods at irregular intervals, so LASCO/EIT operates with increased telemetry for much of the time. The bulk of this extra telemetry is typically used to obtain full-disk, full-resolution EIT images with a higher cadence than can be achieved with the nominal telemetry allocation.

Most of the image compression routines used by LASCO were discussed earlier (Brueckner *et al.*, 1995). One significant addition to this set is a wavelet based compression scheme known as H-Compress. For LASCO the H-Compress software was developed from the original H-Compress by R.L. White. The software implementation for LASCO was modified to specifically use H-compress on a 32×32 pixel block with 16 bits per pixel. LASCO images are generally larger than 32×32 pixels in size so they are broken into individual 32×32 pixel blocks prior to compression to avoid losing an entire image if transmission errors occur. The individual blocks are then reassembled on the ground into complete images. A detailed discussion of the compression scheme is presented elsewhere (White and Percival, 1994).

There are a number of levels of LASCO data products that reflect different amounts of processing. The lowest level data, Level-0, is the original data stream as it arrives from the spacecraft. These separate packets arrive at Goddard Space Flight Center and are transferred to NRL in two ways. Initial data arrives in near-real-time (NRT) and are used to generate the quick-look data set as the data are received. This data set is often missing complete images as well as parts of images. Subsequent retransmission of the down linked original data to NRL is generally more complete but occasionally data that was present in the quick-look data set is missing in the re-transmitted data and must be retrieved from the quick-look data set. The Level-0 data is processed from spacecraft packet data into fits files of individual images and forms the Level-0.5 data set. Beyond the collection of information about the observation into the FITS header and the assembly of the image into a FITS file, rectified with solar north "up", no corrections are applied to the Level 0.5 images.

As mentioned above, analysis of LASCO data has proceeded since launch using the preflight calibrations or those derived during the early portion of the mission as necessary for specific analysis requirements. The calibration efforts discussed in this paper have been used to generate the next level data product, Level-1. The Level-1 data set is generated by applying the complete set of calibrations discussed below to the Level-0.5 data set (see Section 11).

3. Characteristics of the Flight CCD

The LASCO CCDs are Textronix 1024 × 1024 pixel devices with 21 μm^2 pixels. These devices have four readout ports, one on each corner of the array. The CCDs are operated in multi-phase pinned (MPP) mode. Although MPP mode reduces the full well capacity of each pixel it minimizes noise generated thermally and by energetic particles. This section addresses only those CCD characteristics that impact the photometry. Other electrical properties of CCDs have been addressed elsewhere in more detail (Janesick, 2001).

3.1. Quantum efficiency

The quantum efficiency (QE) of the C3 flight CCD was measured at NRL. The basic experimental setup involved a light source, a set of 15 narrow band filters (FWHM ∼100 Å) covering the 4000 to 11 000 Å range, two photo-diodes, and an integrating sphere. A vacuum system was used to allow the CCD to operate at anticipated flight temperature (∼−80 °C) during these measurements. The NIST traceable photo-diode was used to place the measurements on an absolute scale while a working photo-diode was used to monitor variations in the lamp intensity and so account for lamp fluctuations in the final results. The uncertainty in these measurements is ∼3% for the QE and ∼5–10% for the wavelength.

The temperature of the CCD during the SOHO mission is ∼−74 °C rather than the ∼−80 °C used during the pre-flight QE measurements. A set of post-launch QE measurements was made by SiTE Inc. using a LASCO flight spare CCD at three different temperatures to estimate the impact of temperature variations on CCD QE. The QE of the CCD was measured at +22, −30 and −64 °C as a function of wavelength. These temperature dependent measurements were obtained with a scanning monochromator using a bandpass of 100 Å over a 3500–11 000 Å wavelength range. The QE results at the above temperatures provide an estimate of the ratio of the flight CCD QE at ∼−74 and ∼−80°C. Using the ratio of estimated QE at these latter temperatures the QE of the flight CCD was estimated at −74 °C. Figure 3 shows the corrected QE of the flight CCD plotted as a function of wavelength. Although the estimated variation of the QE between −74 and −80 °C is within 5% over most of the wavelength range this correction has been applied to the photometric calibration.

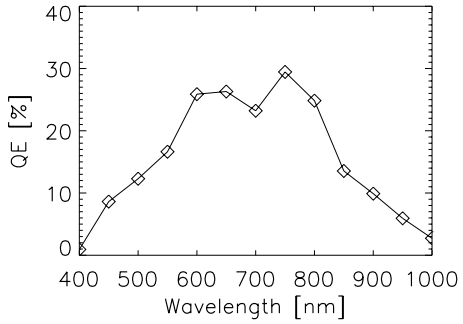

Figure 3. QE of C3 flight estimated at −74 °C. See text for error estimates.

3.2. OFF-SET BIAS, DARK CURRENT, AND OUTPUT PORT GAIN

To ensure that the A/D converter in the CCD camera always measures a positive voltage, the four off-chip output amplifiers connected to the four output ports on the CCD are biased with a positive voltage. The amount of the bias is different for each of the four readout ports and the value for Port C is determined periodically in flight. This level must be subtracted from the measurements prior to corrections for exposure time. In addition, as is characteristic for measurements with most electronic detectors, the dark current level, if significant, must be determined and subtracted from the observed CCD signal. Finally, the relative gain of the four on-chip output amplifier must be determined. These relative gain values are used when comparing measurements made with different output ports. Note, however, that after the initial commissioning exercises, only Port C is used for the scientific observations by the C3 instrument.

The CCD offset bias and dark current values have been periodically measured throughout the SOHO mission. The C3 offset bias has increased in flight although the cause of the increase is not understood. We note that for the four LASCO and EIT cameras, which all use the same electronics design, all show different behavior, with the EIT showing no increase. Figure 4 gives the offset bias as a function of time

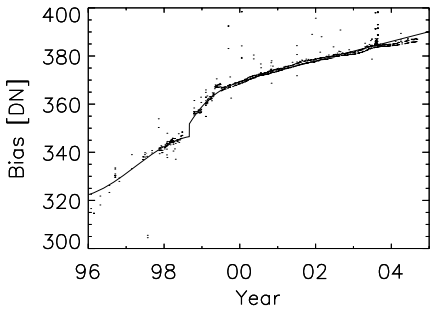

Figure 4. CCD readout port C bias during SOHO mission.

TABLE II
C3 readout port properties.

Read port	Bias [DN]	Relative gain
A	364	1.02
B	540	0.94
C	317	1.00
D	283	1.03

for Port C of the C3 CCD. The break in the curve occurred during the period when contact with the SOHO spacecraft was lost. The fit to the offset bias is computed in three different ways, which give essentially the same values.

The first technique is to use the average of the under-scan pixels, which are the first 20 pixels in the serial register before the start of the imaging pixels that have been shifted into the serial register from the parallel register. The second is to use dark exposures with a zero second exposure time. The accuracy of these methods could be affected by light leaks around the shutter and cosmic ray particles that would generate signal during the readout. While this signal can be estimated, the third method completely avoids this problem. In this method the CCD serial register is clocked in a direction away from the output node. Thus, no video information is transferred onto the output node and the digitized output is only the offset bias and system noise. The bias values before and after the 1998 interruption are fit to separate polynomials. Table II gives the offset bias at the beginning of the mission for all the output ports. Port C was chosen as the primary readout port during SOHO instrument commissioning based on its overall noise performance.

In order to reduce dark current, to mitigate against the effects of radiation damage in the bulk silicon, and in particular to optimize the charge transfer efficiency, the CCD was operated at a low temperature ($\sim -74^{\circ}$C). As a result, the accumulation of thermal electrons, or dark current, is very low. A standard sequence of dark exposures (one in which the shutter is kept in the closed position) of 0, 60, and 300 s was run periodically throughout the mission. This time is the amount of time between the end of the CCD clearing cycle and the start of the readout. A median value is determined for images at each exposure time, the bias is subtracted, and the slope of the results versus exposure time yield the dark count. The dark count is effectively zero for C3.

Differences in on-chip amplifier gain must be determined in order to compare the signals from the four readout ports. This has been done in the laboratory before flight and in-flight. In the laboratory, measurements were made of a lambertian light source through all the readout ports. In-flight, measurements of the door diffuser (see below) confirmed these results. These relative gain values appear in Table II and, although all are nearly identical, these values are used to correct the pre-flight intensity calibration for comparison with the in-flight calibration.

3.3. CCD CHARGE TRANSFER EFFICIENCY

In transferring the charge across the silicon, an incomplete transfer of the photo-electrons from one pixel site to another can occur. Traps in the bulk silicon, for example, can lead to the removal of some of the charge from the charge packet. Since the parallel register is different from the serial register, the ability to transfer charge can be different in the two directions. The charge transfer efficiency (CTE) is represented by a single number giving the average efficiency in the form (Signal Out)/(Signal In) = CTE. The LASCO camera is able to determine the CTE in flight, by using the "Extended Pixel Edge Response" (Janesick, 2001). In this technique the first pixel in the overscan is compared to the baseline established by the remaining pixels in the overscan region. To determine the serial transfer, we look at pixel 1045 and compare it to the input signal from pixel 1044 (the last column of the imaging array). The baseline is obtained from pixels 1045–1143. No degradation of the CTE has been detected in flight. Both vertical and horizontal CTE is better than 0.999999 for signals greater than 0.1 of full well. The read noise was determined to be ∼5–7 electrons.

3.4. PHOTON TRANSFER

A very convenient way to obtain the important CCD camera parameters is through a technique called the photon transfer curve (PTC). In this technique, the log of the signal is plotted against the noise associated with that signal level. If the noise is due to photon statistics, then the curve is linear, with the noise being proportional to the square root of the number of electrons generated. Equating the actual slope of the curve to 0.5, the system calibration (electrons per DN) can be determined. The system noise and the full well are also obtained from this plot. For the C3 CCD the number of electrons per DN is ∼13 and the full well capacity is approximately 160 000 electrons.

Two procedures are used to obtain the PTC. One is to take two exposures of the same scene at the same exposure time and then to take a series of exposure times. The difference between the two images at the same exposure time yields the noise. The second technique both clears and reads out the CCD while it is being exposed (to solar illumination). Thus, each column of the CCD sees the same integration through the scene and gives 1024 samples, from which the standard deviation can be computed. This technique gives a 24.2 s exposure (50 kHz serial clock). Again, no change has been seen in the calibration parameters since launch.

3.5. HOT AND DARK PIXELS

For most CCD detectors, there can be a certain number of pixels that have high dark count rates due to defects in the devices that form each pixel. There are also pixels

that show limited or no sensitivity to illumination and so are effectively dark. The C3 flight CCD was selected from a set of detectors based on a variety of metrics, two of these involve minimizing the number of hot and dark pixels. This section discusses the long-term behavior of these properties for the flight CCD.

Hot pixels were examined using 60s dark exposures similar to those used to determine dark current and offset bias values. However, given the longer exposure time cosmic ray events had to be excluded in the analysis. Maps of hot pixels were made for 1 year periods during the SOHO mission. Here, dark images measured at various times during the selected 1 year period were compared in order to identify hot pixels and exclude cosmic rays. In general, the count rates from most of the pixels had values clustered around the bias value since the dark current is effectively zero. However, some pixels showed higher count rates and those in the top 20% of the count rate distribution were examined in this analysis.

The results of this study showed two basic results. First, roughly 1.5 pixels per 1000 ($\sim$0.15%) were considered to be hot pixels. Second, these hot pixels showed an excess dark rate of $\sim$2 DN for a nominal C3 exposure ($\sim$20 s duration). For studies where photometry is important (e.g., long-term studies of the F corona) where the coronal intensity is summed over a significant region of the C3 FOV, this results in an excess of $\sim$10 DN pixel^{-1} s^{-1}.

Dark pixels were examined by use of calibration lamp images. The calibration lamp illuminates the back of the CCD shutter and reflected light from this surface passes through a filter and polarizer. The illumination is not uniform so the image is not flat but this is not necessary. A procedure similar to that used in the hot pixel study identified pixels with a response below a certain fraction of the local average value. For the dark pixel study, dark pixels where chosen as those with a sensitivity $<$10% of the average. Over the course of the SOHO mission $<$80 pixels ($\sim 8.0 \times 10^{-3}$%) have been shown to fall into this category.

Given the insignificant contribution to the errors in intensity no correction have been applied for either hot or dark pixels.

3.6. Fixed pattern noise

A common characteristic of CCD cameras is referred to as fixed pattern noise, which arises from slight deviations in the fabrication of the pixel structure on the CCD causing some pixels to be very slightly smaller and others larger. This forms a regular pattern of varying intensities. We have examined C3 images to see if this represents a significant noise contribution. The method used involves generating a difference image between the original and boxcar smoothed image of the corona (un-sharp mask). An FFT of the difference image is examined to show the presence of any power in the resulting spectrum. Our analysis does reveal an extremely weak fixed pattern but it is insignificant compared to other noise sources so no correction is applied to the processed coronal images.

3.7. Summary of CCD properties

The CCD QE was measured pre-flight at $-80\,^{\circ}$C but the in-flight temperature is $-74\,^{\circ}$C. Using a flight spare CCD temperature variations in the QE were measured and used to estimate the flight CCD QE at the in-flight temperature. The dark current was measured and found to be zero at the in-flight temperature. The time variation of the off-set bias for the primary output port of the CCD (Port C) has been measured (320–390 DN for 1996–2005) and is a required value for photometric calibration. The measured CTE is 0.999999 and the read noise is 5–7 electrons. Photon transfer techniques provide the number of electron per DN as 13 and a full well capacity of $\sim$160 000. Hot and dark pixels were examined and found to be $\sim$0.15 and 8.0×10^{-3}% of the CCD pixels, respectively. A weak fixed pattern noise was detected but at a level below other noise sources. Given the small contribution of hot and dark pixels as well as the weak fixed pattern noise no corrections were applied for these noise sources.

4. Photometry

This section describes the impact of the optical components of C3 that contribute to the photometric calibration and the various pre-flight and in-flight methods used to derive this calibration. Results from pre-flight and in-flight measurements are examined and compared.

4.1. Instrument components

The primary instrument components that are important to the photometric calibration are the color filter transmission curves, the transmission of the C3 lens, the sizes of the limiting apertures. A detailed discussion of these characteristics is presented in the following sections. The spectral response characteristics of the CCD were discussed in the previous section.

The coronagraph optical train includes a set of five broadband color filters mounted in a wheel, one of which is always in the beam. A narrow band Hα filter is mounted in a second wheel which also holds the polarizer filters (see below). These color glass filters were fabricated by Andover Corporation. The spectral transmission of these filters is shown in Figure 5.

Here, we define the photometric calibration in terms of a ratio of the coronal brightness to the average full disk solar brightness within the passband of the various filters. As a result, properties of the instrument that do not vary with wavelength need not be considered. Two components of an optical instrument that generally impact a photometric calibration are the limiting aperture and the transmission of the lenses in the optical train. The limiting aperture in the C3 instrument is the Lyot Stop shown in the optical layout (Figure 2) and has a diameter of 3.0 cm. Before

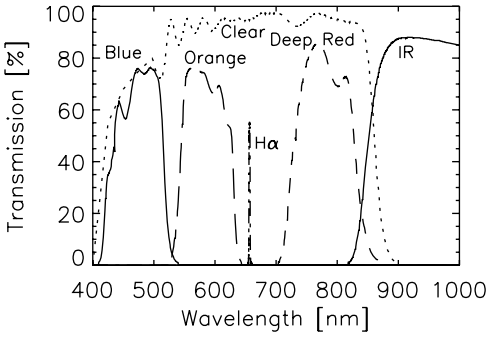

Figure 5. Spectral transmission of the C3 filters.

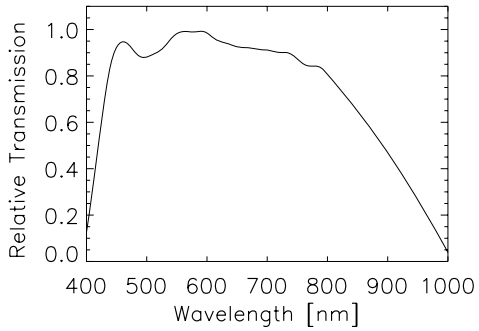

Figure 6. Overall transmission of the LASCO C3 lens.

flight, the overall transmission of the various lenses shown in Figure 2 was measured with a telephotometer and estimated to be spectrally flat over the wavelength range of the filters (4200–11 000 Å). However, difficulties in calibrating the DeepRed and IR C3 filters indicated the need to measure the wavelength dependent transmission of the C3 lenses. This was done using the C3 engineering unit that contained flight-spare lenses and so provides a good estimate of the overall transmission of the flight C3 lenses. The relative transmission of these lenses appears in Figure 6 and this was used in the photometric calibration.

4.2. Pre-flight calibration methods and results

The LASCO pre-flight calibration measurements were obtained in the Solar Coronagraph Optical Test Chamber (SCOTCH) at NRL in April, 1994. During these measurements, the cameras were maintained between -30 and $-40\,^{\circ}$C under high quality vacuum (10^{-6} Torr). Throughout the calibration testing, the instrument viewed two separated opal glass plates, uniformly illuminated from behind. The laboratory apparatus discussed here was used for numerous tests presented in the following sections.

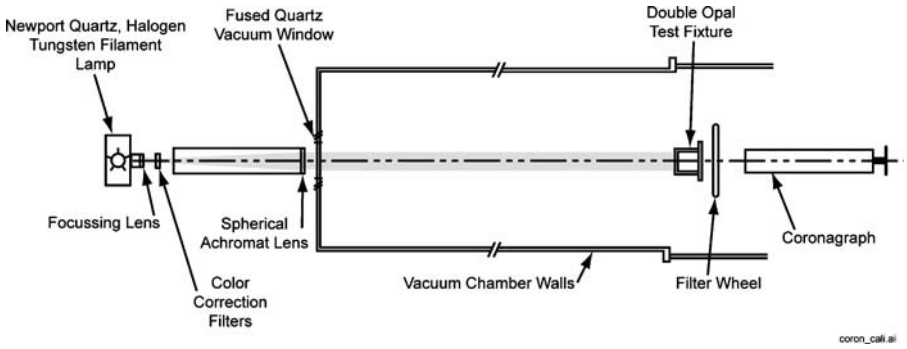

Figure 7. Optical layout of the laboratory calibration test set-up.

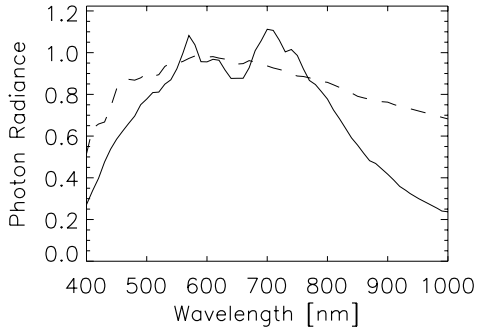

Figure 8. Spectral radiance of the calibration opal (solid line) and the solar disk center radiance spectrum (dashed line) scaled to an overall best fit to the laboratory lamp spectrum.

The light source used for the laboratory calibration was a servo-stabilized, Newport 50 watt tungsten-halogen bulb (∼1%) with a concentrator system that illuminated a field diaphragm in the lamp housing. The Newport lamp was focused on a pair of 12 cm diameter opals that produced a relatively uniform illumination pattern at the second opal viewed directly by the coronagraph during the calibration. Color filters were placed near the field diaphragm to obtain a nearly solar spectrum. Figure 7 shows a basic layout of the laboratory apparatus. The spectral radiance of the calibration opal was measured using a filtered spot meter and a spectroradiometer. Figure 8 shows the measured spectral radiance of the test opal for C3 along with the disk centered solar radiance.

The lamp spectrum (Figure 8) was a relatively good match to a 3200 K blackbody curve. To adjust the spectral content to more closely match the coronal spectrum, a 3.9 mm thick Corning number 5900 blue filter and two 1 mm thick Corning 1–75 infrared rejection filters were used to produce a match to within 25% of the solar spectrum from 420 to 820 nm. To more closely match the coronal brightness expected in the C3 FOV, neutral density filters were used when the coronagraph was calibrated. The C3 neutral density filter did slightly change the spectral content

of the opal radiation. The color and neutral filter transmittance were measured with a Cary spectrophotometer at NRL.

Two instruments were used to calibrate the opals; a spectroradiometer (International Light, model IL1 700/586D, 1 nm bandpass, 300–800 nm range) and a spot telephotometer. Order sorting filters reduced second order spectral contamination. A silicon photodiode, a Keithley electrometer, and an IBM PC were used to measure the spectroradiometer output. The encoder measured wavelength was calibrated using a Hg Penray lamp. The absolute calibration was determined using a NIST traceable source (Licor 1800-02, $\sim$4% between 350 and 1000 nm).

The spot telephotometer independently verified the opal calibration. Three internal filters (photopic, red and blue) were used and provided a direct measurement of the opal brightness in photometric units and a measurement of the color temperature. The calibration of the unit was verified using the Licor source, a standard photometric source and its internal calibration source. The measurements between the spectroradiometer and the telephotometer of the opal brightness were in agreement to within $\sim$10%. Prior to flight, an image was obtained through each color filter of the opal glass diffusing screen.

The results of the pre-flight photometric calibration are presented in Section 4.4. The results were used to calibrate images prior to the completion of the in-flight calibrations discussed in the next sections. We have subsequently re-evaluated the pre-flight results to correctly account for solar limb darkening and more accurately account for the CCD QE and filter and lens transmission curves.

4.3. IN-FLIGHT PHOTOMETRIC CALIBRATIONS

The in-flight calibrations use two types of measurements. The first involves on-board light sources; the calibration lamp that illuminates the CCD shutter and a diffuser window installed in the C3 door. These measurements are discussed in Section 4.3.1. The second (and primary) type of measurement used star observations. This analysis is described in Sections 4.3.2 and 4.3.3.

4.3.1. *Calibration Lamps and Door Diffuser*

Redundant on-board calibration lamps are mounted behind the CCD shutter. When powered, the lamp illuminates the rear of the shutter which then illuminates the CCD through any combination of color and polarizer filters. These lamps provide a light source for liveness tests of the CCD without opening the camera shutter. They also have been used to examine degradation of the color filters and polarizers separately from the other C3 optical elements. The C3 door also has a diffuser disk that is illuminated by the Sun when the door is closed. Light from the door diffuser passes through the entire C3 optical system in addition to the color and polarizer filters and so provides calibration information and has been used to examine the long-term stability of the optical system.

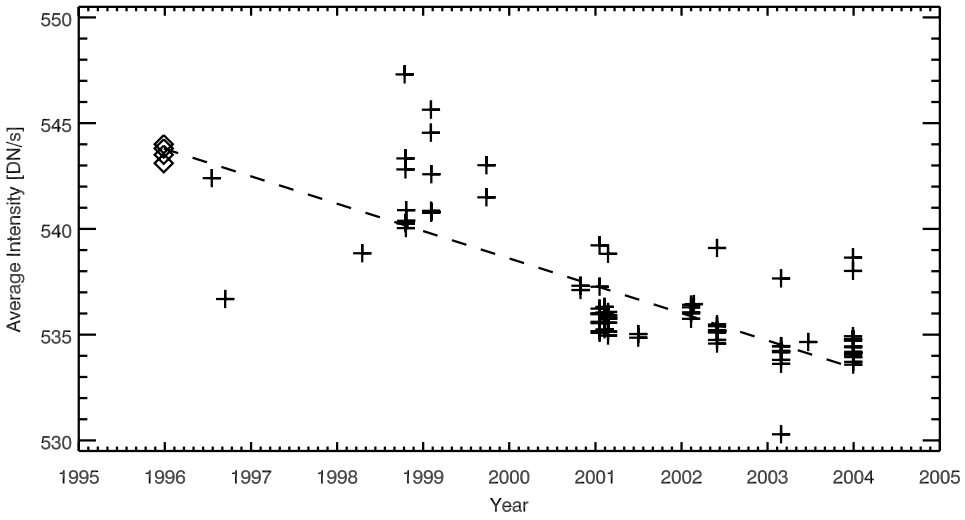

Figure 9. Calibration lamp intensity measurements from 1996 to 2002. The diamonds are from read port D and the pluses are from read port C.

Measurements of these sources have been taken throughout the SOHO mission and provide a periodic measure of the instrument sensitivity as well as verification of CCD properties and degradation. For example, one polarizer filter failed during 1998 when contact with SOHO was lost and the status of this filter was verified with the use of the calibration lamps and door diffuser. Other uses of these on-board facilities include, the evaluation of dark pixels on the CCD, the measurement of the relative gain of the CCD output ports, and the evaluation of the CCD CTE (see Section 3.3).

Calibration lamp images have also been used to examine the source of the minor decrease in the clear filter sensitivity discussed below (see Section 4.3.4). Figure 9 shows the intensity of the calibration lamp at various times throughout the mission through the clear filter. The measurements in late 1998 show significant scatter that is likely due to heater temperature variations during the SOHO recovery period. During the period 1996 through 2003, intensity measurements show a slight decline of $\sim$1.7% ($\sim$0.25% per year). These results will be discussed further in Section 4.3.4.

4.3.2. *Solar and stellar magnitude based calibrations*

As part of a recent paper (Mallama, Wang, and Howard, 2002), LASCO C3 observations were used to study the photometry of Mercury. Analysis of the C3 observations produced V photometry of Mercury when it was between $\sim 0.5^\circ$ and 8° from the Sun's center as well as a detailed calibration of the C3 orange filter. The LASCO passband for the C3 orange filter is 530–640 nm. Transformation from instrumental magnitudes to V-magnitudes was accomplished by measurement of the intensity

of bright stars in archival images, using the same aperture and annulus sizes as for Mercury. The conversion method (Hardie, 1962) used stars that were redder and bluer than Mercury to insure reliable interpolation. Each of the transformation stars was measured in multiple images of each color filter and a median taken. This minimizes the chance of a stray cosmic ray affecting the results. The transformation equations used to convert the Mercury observations to the UBV system are shown as follows:

$$V = O_{\mathrm{LASCO}} + \alpha(B - O)_{\mathrm{LASCO}} + \beta \tag{1}$$

$$B - V = \gamma(B - O)_{\mathrm{LASCO}} + \delta \tag{2}$$

where B and O refer to the blue and orange LASCO *magnitudes*, equivalent to -2.5 times the logarithm of counts per second and corrected for vignetting, $\alpha = 1.439$, $\beta = -1.080$, $\gamma = 0.437$, $\delta = 9.021$.

To determine the calibration factors for the orange filter, an estimated response is derived of the full disk of the Sun imaged by C3. For the sun viewed from earth $V = -26.74$ and $B - V = +0.65$. Using Equation (2), $(B - O)_{\mathrm{LASCO}} = 1.203$ and substituting this value into Equation (1) gives an average estimated count rate over the full solar disk of 3.372×10^{14} DN s^{-1}. The image of the Sun viewed from Earth would cover a disk of area $((960''/(56''/\mathrm{pixel}))^2 x\pi) = 923.2''$ pixels. The resulting estimated count rate, when the observed brightness is the full disk solar brightness, is $3.653 \times 10''$ $[(\mathrm{DN\,(s\text{-}pixel)}^{-1})/(B/B_{\mathrm{Sun}})]$ since $B/B_{\mathrm{Sun}} = 1$ in this case. The orange filter calibration factor is therefore the reciprocal of this value, 2.80×10^{-12} $[(B/B_{\mathrm{Sun}})/(\mathrm{DN\,(s\text{-}pixel)}^{-1})]$. This value agrees reasonably well with the value derived from the stellar spectra method discussed in Section 4.3.3.

4.3.3. *Solar and Stellar Spectra-based Calibrations*

In order to determine the in-flight photometric calibration of all the C3 color filters we used the 13-color stellar photometry (Johnson and Mitchell, 1975, 1977; Johnson, 1980). That work covers 1300 stars of which ~130 pass through the C3 field-of-view during the course of a year. From this set we have examined ~ 60 stars that we have found to be suitable and that have been observed numerous times throughout the mission. This analysis provides both the photometric calibration and a measure of the stability of this calibration with time. In this section, we discuss the general method used to derive the calibration factors. In the following Section 4.3.4 we apply this method to the first 7 years of LASCO data.

Using the 13-color stellar photometry catalogue we have generated an estimated spectrum of each star in this catalogue that passes through the C3 field-of-view. This set of stars was reviewed and a subset of these stars was determined for use in calibration. To calculate the estimated total brightness of a particular star through a given filter, the estimated spectrum of the star is convolved with the wavelength

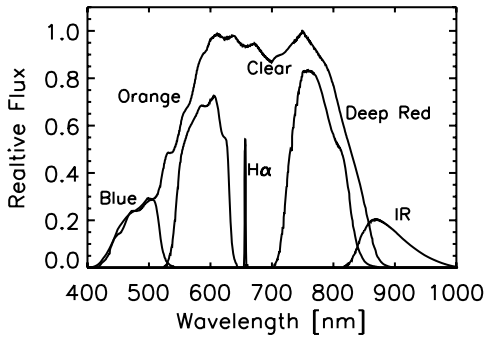

Figure 10. Product of QE, overall transmission, and solar spectrum for various C3 filters.

dependent QE, the color filter, and lens transmission of C3, where we approximate the following integral with a sum,

$$B_{\text{Star}} = C \int I_{\text{Star}}(\lambda)\text{QE}(\lambda)T_{\text{Filter}}(\lambda)T_{\text{Lens}}(\lambda)\,\mathrm{d}\lambda$$
$$= C \sum I_{\text{Star}}(\lambda)\,\text{QE}(\lambda)T_{\text{Filter}}(\lambda)T_{\text{Lens}}(\lambda)\Delta\lambda \qquad (3)$$

Here I_{Star} is the stellar brightness, QE(λ) is the CCD quantum efficiency (Section 3.1), T_{Filter} is the filter transmission, T_{Lens} is the overall C3 lens transmission, and C is a wavelength independent proportionality constant. For each filter, the curves defined by the product in the argument of the integral above varies significantly with the stellar spectrum. The final calibration factor converts (DN s^{-1}) to solar brightness ratios (B/B_{Sun}). Consequently, the limb darkened solar spectrum also must be convolved with the CCD QE and filter and lens transmission curves to calculate the estimated solar brightness through each filter, as if the full solar disk were imaged by C3. The product of I_{Sun}, QE, and the transmission curves appear in Figure 10. The proportionality constant, C, is the same for all cases since it depends on the area of the C3 limiting aperture and all other non-wavelength dependent properties of the instrument.

Using the total fluxes associated with the above stars and the various filters, we determine the ratio of the photon flux of the stars to the photon flux of the Sun through each filter with the result having units of $[B/B_{\text{Sun}}]$. Using C3 observations of stars through the five filters, total count rates ([DN (s-pixel)$^{-1}$]) associated with these stars are then measured. Primarily, this involves a background subtraction, normalization with the reported exposure time, and a vignetting correction (see Section 5). Exposure factor corrections were not used in these calculations since these corrections are generally very small and have been calculated only for the clear filter observations (see Section 8).

A critical step in determining the calibration factor for a given filter is the use of the C3 pixel as the angular subtense for the star since the estimated stellar irradiance

TABLE III
Comparison of pre- and in-flight calibration factors $[(B/B_{\mathrm{Sun}})/(\mathrm{DN\,(s\text{-}pixel)}^{-1}) \times 10^{-12}]$.

Filter	Pre-flight (Corr.)	Pre-flight	Stellar mag.	Stellar Spec.	in-flt/pre-flt
Blue	10.3	11.1	–	9.75	0.87
Orange	2.86	3.60	2.80	2.97	0.80
Clear	0.503	0.597	–	0.619	0.97
Red	1.94	2.26	–	2.58	1.13
IR	2.64	6.70	–	8.87	1.32

is treated as a uniform brightness over a single pixel even though the star's image extends over a number of pixels. Consequently, the observed count rate of the star is treated as if it occurred within a single pixel. Results from this analysis appear in Table III.

No corrections have been made for the variation of the SOHO–Sun distance as none is required. While it is correct that the irradiance of the Sun will vary with changes in the SOHO–Sun distance, the brightness of the Sun does not change (Gray, 1992). That this is the case can be confirmed with two arguments both of which involve the nature of brightness measurements. First, the wavelength dependent average solar brightness (photons per cm^2-s-steradian) is derived from the average, limb darkened, solar spectral irradiance (photons per cm^2-s) and the subtense of the solar disk (steradians) as viewed from the measuring instrument. As the instrument moves from 1 AU to the SOHO orbit the solar irradiance increases by a factor of $R^2_{1\mathrm{AU}}/R^2_{\mathrm{SOHO}}$. However, the subtense of the solar disk increases by the same amount. As a result changes to the solar irradiance and the subtense cancel one another when deriving the solar brightness as the ratio of the irradiance to the subtense.

The second argument involves the object of the LASCO measurements, the determination of the coronal brightness. The brightness of a small patch of the corona (say one C3 pixel of $\sim 4.2 \times 10^{-6}$ sr) is due to the scattering of photospheric light by dust and electrons along the line of sight associated with this patch. As the distance from SOHO to the location of this patch of corona (e.g., to the plane of the sky at the Sun) changes, as it does throughout the year, the physical size of this patch varies slightly. However, the distance from the Sun to the points along this line of sight does not change significantly so that the illumination of the patch is effectively fixed. Assuming that the solar irradiance does not vary and that the observed scattered light originates near the Sun, a given line of sight dust and electron density profile will produce a coronal brightness that is unchanged by distance. The reason is the same as with the first example. As SOHO moves away from the Sun the physical size of the patch, and the amount of scattering material viewed by the instrument, increases but the amount of light from this material that

TABLE IV
Final LASCO C3 calibration factors $[(B/B_{\mathrm{Sun}})/(\mathrm{DN\ (s\text{-}pixel)}^{-1}) \times 10^{-12}]$.

Filter	Cal. factor	Sigma (%)	No. of stars	No. of samples
Blue	9.75	1.21	59	2,157
Orange	2.97	0.99	60	4,895
Clear	0.619	0.73	62	82,662
Red	2.58	1.13	59	1,737
IR	8.87	1.44	59	1,295

enters the instrument decreases by the same amount so the observed brightness remains unchanged.

To compare the calibration factors determined from the star observations with the pre-flight values, a number of corrections were applied to the pre-flight analysis. These corrections were in addition to the corrections associated with the convolution of the CCD QE and filter transmission with the laboratory light source discussed above. First, the solar spectrum used in the pre-flight analysis was the disk center radiance rather than the average radiance over the entire disk. This is an important correction since it includes the wavelength dependent limb darkening and the limb darkened solar spectrum is required in calibrations based on the star spectra. Second, different CCD output ports, with different relative gains, were used during pre-flight calibrations than have been used in flight (see Section on 3.2). As with the solar and stellar spectra, the laboratory light source spectrum is convolved with the CCD QE, color filter, and lens transmission curves to determine the corrected pre-flight calibration factors. A comparison of pre-flight and in-flight calibration factors appear in Table III and the details of the in-flight analysis appears in Table IV (see Section 4.4).

4.3.4. *Time Dependent C3 Sensitivity*

In order to examine the stability of the observations through the five C3 filters, star intensity observations were analyzed year-by-year from 1996 to 2003. The brightness of each calibration star that passed through the C3 FOV is determined for each filter as discussed in the previous section. The observed count rates for each star are averaged for a given year and plotted against the calculated brightness. An example of these plots appear in Figure 11 for the clear filter. The slope from a linear fit to these points yields the calibration factor. An important note about these plots for the various filters is that the error bars for the clear filter are significantly smaller than for the other filters. This is largely due to the fact that the clear filter has had far more observations than any other filter.

The resulting yearly calibrations of each filter was examined for trends. Only the results for the clear filter were of high enough quality to determine the presence of a drift. The results appear in Figure 12 and show a gradual reduction in sensitivity

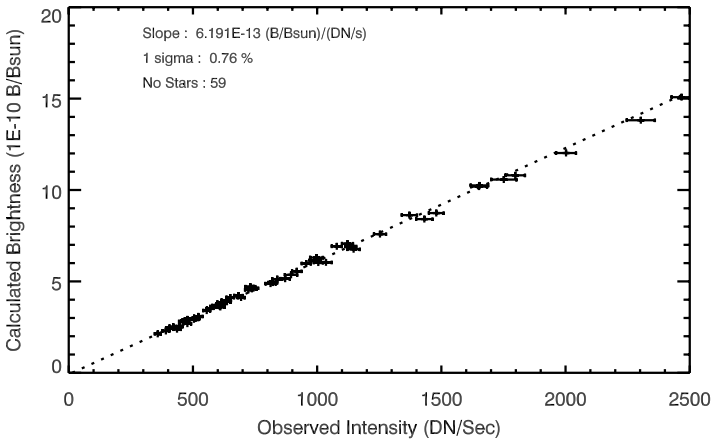

Figure 11. Star brightness versus observed star intensity through the clear filter.

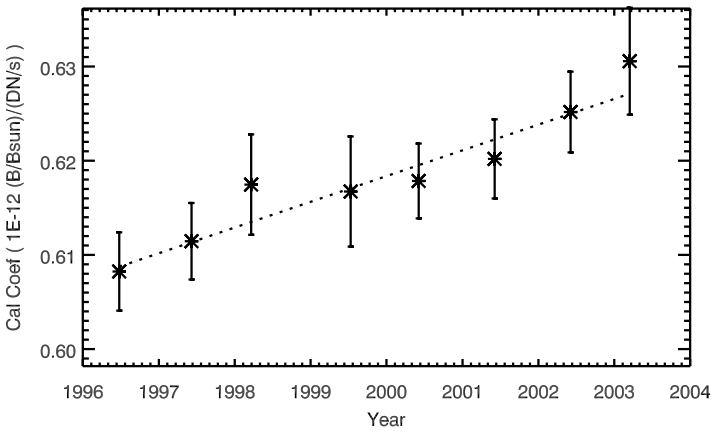

Figure 12. Clear filter calibration factors for years 1996 through 2003.

of ∼3% over the 7 year period examined. Although this is a very slight drift, a time dependent calibration is applied to the C3 Clear observations during Level-1 processing. A more detailed discussion of these analysis techniques and results is discussed in a separate paper (Thernisien, Morrill, Howard *et al.*, in press).

4.4. SUMMARY OF PHOTOMETRIC RESULTS

A comparison of pre-flight and in-flight calibration factors appears in Table III. The mission averaged calibration factors and errors derived from stellar observations appear in Table IV. The pre-flight corrected column in Table III are corrected to CCD port C, accounting for the effects of limb darkening of the solar spectrum, and incorporating the wavelength dependence of the C3 instrument. The variation of the C3 Clear calibration factors with time during the mission was shown in Figure

12 and shows only slight degradation during the mission. Since there are fewer stellar observations with the other filters, scattering in the calibration of these filters is greater than with the Clear filter and so any slight trends in the degradation in these filters is within the calibration errors.

5. Vignetting

To create an artificial eclipse condition, the C3 coronagraph contains an external occulter which shades the objective lens from direct solar radiation. C3 is significantly over-occulted to improve the stray light rejection. As a result, coronal images are vignetted inside 10 R_{Sun} by this occulter. One benefit to this vignetting is that as the brightness of the corona rapidly increases in intensity toward the center of the coronagraph FOV, the instrument sensitivity decreases rapidly. This effectively increases the dynamic range of C3 allowing weak signals in the far field to be observed while the signals near the occulter remain within the dynamic range of the detector.

5.1. Pre-flight laboratory measurements and results

A 2-dimensional vignetting function was determined before launch from a flat field image. This image was generated using the diffuse light source discussed in Section 4. These results show that the vignetting begins at $\sim$10 R_{Sun} and drops to zero at $\sim$3.8 R_{Sun}. The support pylon which typically appears in the lower left quadrant is also a source of vignetting.

Early in the mission a re-examination of the laboratory results and setup indicated the possibility that the diffuse light source used to measure the pre-flight vignetting function had been front-illuminated by the heat rejection mirror shown in Figure 2. This excess illumination could have produced an enhancement in the central part of the vignetting function. As a result, extensive efforts were made to confirm the pre-flight vignetting function.

5.2. In-flight stellar measurements and theoretical estimates

In order to validate the pre-flight vignetting function a series of star intensity measurement programs were undertaken. The C3 coronagraph images show a multitude of stars (see Figure 1) and these have been used in a number of studies to determine the vignetting function in addition to instrument photometry (Section 4) and spacecraft orientation (Section 7). There are, however, a number of difficulties with using stars as calibrated sources. In general, a star's magnitude is the primary source of information about a star's absolute intensity.

In determining the vignetting function with stars, the intensity of a specific star is measured as it passes through the C3 FOV. Measurements of this kind are done for a large number of stars in numerous images so that as many locations as possible in the FOV are sampled. The intensities are then normalized to unity in the

region between 10 and 25 R_{Sun} where the objective lens is un-vignetted. However, imaging systems can show a slight decrease in sensitivity with increasing FOV angle (Smith, 2000) so efforts were made to use stars whose intensities could be placed on an absolute scale. This required the use of the calibration stars discussed in the previous section on photometry. Since star based studies were noisy these results were also compared to optical ray trace results. These ray trace calculations included all important optical elements. The star or ray trace results generated a radial sensitivity profile which was rotated through 360° to generate the vignetting function with the center being the center of the occulter.

Figure 13 shows the vignetting profiles from the radial ray trace and the ray trace perpendicular to the occulter pylon. The slight deflection in the region of decreasing sensitivity is due to the presence of the Lyot spot.

In order to determine if a slight decrease in sensitivity with increasing FOV angle exists, the normalized calibration star intensities were examined as a function of distance from the center of the FOV. Figure 13 shows the normalized star intensities over-plotted with the final ray trace results for the upper-left, upper-right, and lower-right quadrants of the FOV. These figures show no significant decrease in sensitivity at large field angles. The lower left panel in Figure 13 also compares the cross section of the pylon from the ray trace results with the observed star

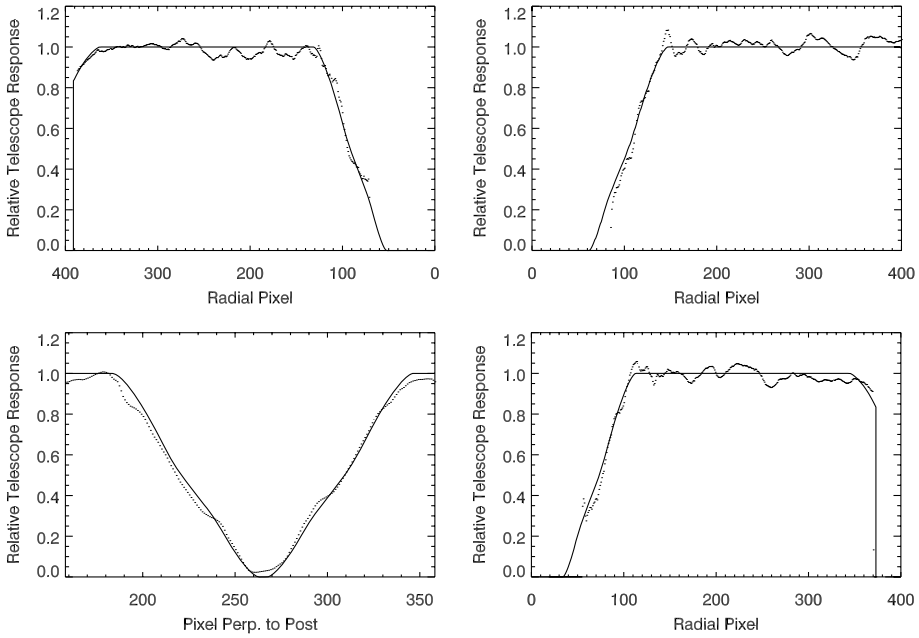

Figure 13. Ray trace model profile fit to average from star observations in three corners (*upper-left*, *upper-right*, and *lower-right*) and perpendicular to pylon (*lower-left*). Note the steep drop in sensitivity near the pylon and the occulting disk and the slight roll off near the outer edge of the FOV prior to the sharp cut-off at the edge of the FOV.

intensities. In the corners of the images the C3 FOV extends to $\sim$32 $R_{\rm Sun}$. A fit to the radial star intensity data shown in Figure 13 was used to generate the portion of the vignetting function at the outer edges. Other results indicated the possibility of a slight relative enhancement on the left side of the FOV. An examination of the intensity variations in seven regions evenly spaced around the FOV by 45° (excluding the pylon) show no significant sensitivity differences exist in the outer portion of the vignetting function so no azimuthal component is included in this vignetting function.

5.3. Summary of vignetting correction results

Pre-flight and in-flight vignetting functions were examined to determine the best vignetting function. The final version is from ray trace results, confirmed by star observations, with a slight modification to the corners near the edge of the FOV. This version agrees very well with the pre-flight function with only minor differences. The final vignetting function is shown in Figure 14.

6. Plate Scale and Geometric Distortion

In order to transform the C3 observations from CCD pixels to a scale proportional to the radius of the Sun, the instrument plate scale (arc-seconds per pixel) must be determined. In addition, geometric distortion of the optical system can result in a variation of the angular size of a pixel over the field-of-view. Although this correction is relatively small the geometric distortion has been determined and the correction is applied in order to improve the accuracy of CME velocity and acceleration measurements.

6.1. Pre-flight laboratory measurements

Laboratory measurements of the instrument plate scale were performed as part of the pre- flight focus and alignment tests of C3. These results agree with the plate scale predicted by optical prescription used in the coronagraph design and development. These focus tests used fine wire meshes and Air Force test patterns placed at the focus of a collimator that illuminated the C3 entrance aperture. For C3 the predicted plate scale of 56 arc-seconds per pixel near the center of the focal plane was measured. No pre-flight measurements of geometric distortion, or changes in plate scale with changes in FOV angle, were performed.

6.2. In-flight measurements

Variation of the plate scale was determined in flight by comparing calculated and observed star positions. Early in the mission a small set of star position was used

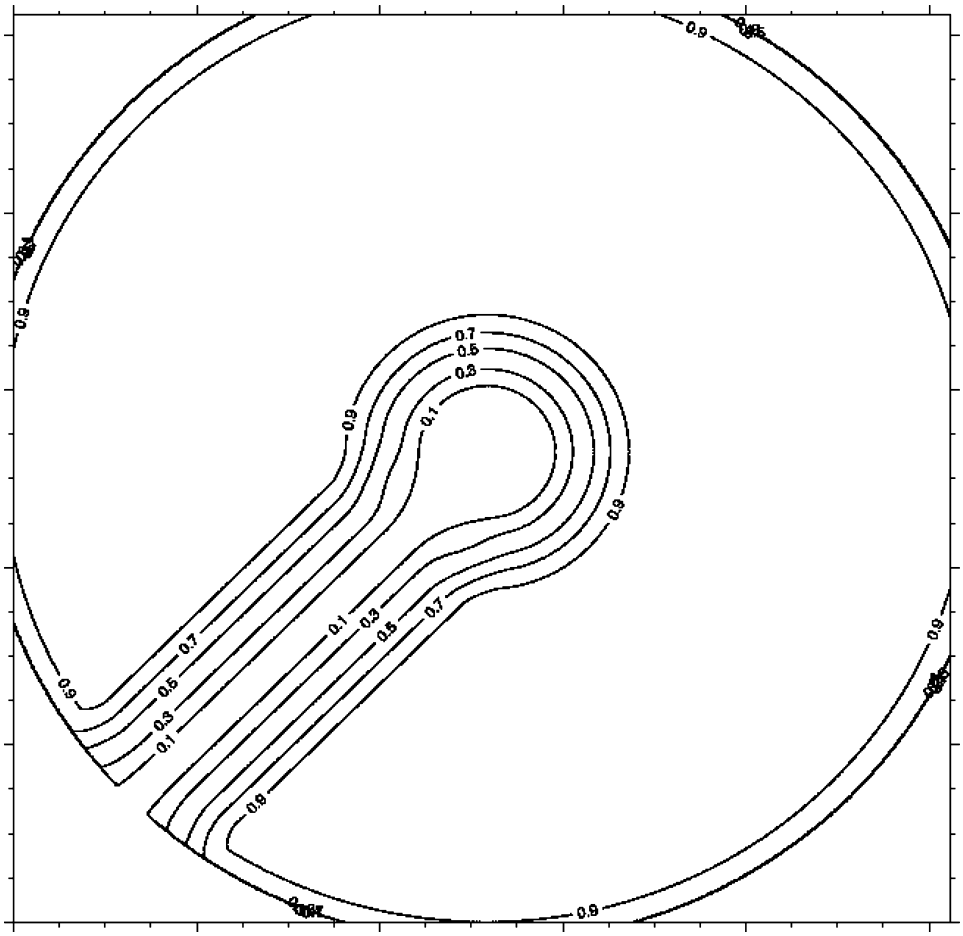

Figure 14. Image of final vignetting function. The x and y axes are in pixels and range from 0 to 1024. The effect of the pylon can be seen in the lower left quadrant and the effect of the occulting disk can be seen at the center. Starting with the contour nearest the center the contour values range from 0.1 to 0.9 with increments of 0.2.

to show that a relatively small pin-cushion distortion was present. In order to better understand the details of the geometric distortion, a comprehensive analysis of observed star positions was undertaken. The results from that study are shown as the solid line in Figure 15 along with the predicted plate scale (dotted line) assumed to be constant across the FOV.

6.3. SUMMARY RESULTS

Pre-flight laboratory measurements indicate the plate scale to be ∼56 arc-seconds per pixel as predicted by the optical prescription. Initial in-flight measurements of

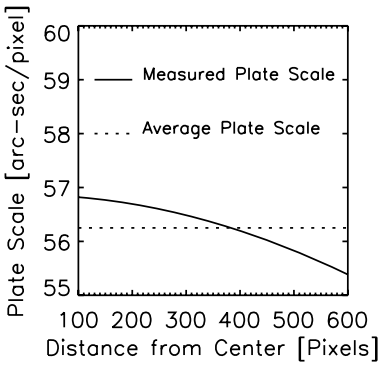

Figure 15. C3 Plate scale versus distance from occulter center.

star positions show the presence of a slight pin cushion distortion. A comprehensive analysis determined the amount of pixel shifting required to correct the natural distortion in the C3 observations to images with a constant plate of 56.25 arc-seconds per pixel. This correction is applied in the Level-1 processing.

7. Determination of Absolute Time, Sun Location, and Spacecraft Orientation

The spacecraft pointing and orientation as well as the absolute time of the images taken are important to the study of CME properties such as position angle and velocity. In order to confirm the accuracy of the on-board clock we have analyzed star observations which are critically dependent on the absolute time, position, and pointing of SOHO.

7.1. Pre-flight alignment activities

Pre-flight alignment was accomplished with the use of a variety of alignment and transfer standards. The optical axis of each LASCO coronagraph was transferred to an external optical alignment cube. The co-alignments between the instruments was within 30 arc-seconds. The LASCO instrument was attached to the SOHO spacecraft with a pair of alignment legs, which had a total pointing range of greater than ± 8 arc-min. This allowed SOHO to be aligned so that the Sun was centered in the EIT FOV and then the LASCO pointing was adjusted so that the Sun was located near the optical axis of the C2 coronagraph. The most critical pointing was to align the LASCO pointing to the external occulter on C2. The C2 internal occulter could then be moved to center the image of the external occulter onto it. The C1 primary mirror had a ± 1 arc-min pointing capability. The C3 had a large mispointing tolerance due to its over-occulting. These fine adjustments were made

TABLE V
Sun center, occulter center, roll angle, and time corrections.

Item	1996–1998	1998–2002
Sun center (x)	518.0 ± 0.5 pixels	518.0 ± 0.5 pixels
Sun center (y)	531.5 ± 0.5 pixels	532.5 ± 0.5 pixels
Occulter center (x)	516.4 ± 0.2 pixels	516.4 ± 0.2 pixels
Occulter center (y)	529.7 ± 0.3 pixels	531.2 ± 0.2 pixels
Roll angle (w.r.t. solar north)	$-0.25 \pm 0.05^\circ$	$-0.25 \pm 0.05^\circ$
Time error (estimated)	~ 1 min day^{-1}	~ 5 min day^{-1}

during the LASCO commissioning phase during the first few months of the SOHO mission.

7.2. Preliminary in-flight determinations of sun and occulter center

Since the external occulter blocks the solar disk from the instrument field of view, the Sun-center and absolute celestial position of the coronagraph images must be determined from other references. Preliminary estimates of the Sun-center position were derived from star positions, the time of the observations, and the reported roll angle of the space craft. The Sun-center position was found to be very close to the occulter center. The results appear in Table V.

Attempts at modeling the positions of stars and a comparison between observations and predicted values indicated significant errors in time or pointing of SOHO. Analysis revealed a time drift of about a minute a day prior to the SOHO interruption. After recovery (October, 1998), the problem with time drifts was found to have increased but this was mitigated by frequent adjustments of the instrument clock.

7.3. Determination of absolute time and spacecraft roll

To determine the Sun-center, roll-angle, and correct observation time, several problems were solved. The most important problem was the effect of timing errors on the overall pointing determination. The final method addressed several difficulties, including knowing the Sun location, the roll angle, the time drifts, (sometimes up to 5 min), and pointing variations due to temperature changes.

The uncorrected absolute time accuracy has three different behaviors during the mission. From launch until June, 1996, the time required no correction. The second period, from June 1996 until the mission interruption in June 1998 showed steady drifts of up to 5 min until the command to transfer the spacecraft time to the

instrument was sent. After the mission interruption the on-board time adjustment no longer worked. A number of methods were considered to correct observed time drifts. The first utilizes the calculated X-position of the Sun center from the stars and corrects the time to place the Sun-center at the proper location. The second method compared the time of the EIT house keeping and science telemetry packets every 10 minutes, during real time data-downlink, to the ground computer time. The difference between these times is the time-offset and should be within ∼15 s. The time-offset calculations were not collected before September, 1997 and occasional gaps occur at later dates. From that time to the SOHO interruption (June 1998) the two methods agreed reasonably well, in contrast to the post- interruption (December 1998—Present) calculations. In this period the EIT time-offsets are considered to be more accurate.

The final solution uses a method that combines the two methods to correct for both time-offset and pointing. Prior to June 1996, no correction is needed. From June 1996 to September 1997, the time correction is inferred from the Sun-center positions. From September 1997 to June 1998, both methods agree. From September 1998 to the present the EIT time offsets are used.

The C2 and C3 pointing and roll corrections were re-calculated from corrected image times and model predictions. Table V shows the roll angle during the mission. A number of changes to the image header results from these corrections. The original time and sun-center values are replaced with the new values and the roll angle is added to the header. The time difference between corrected and uncorrected times are kept in the header as history.

By use of the above time and roll corrections the location of the Sun-center can be determined throughout the mission. In addition, the occulter center was determined at various times during the mission. Table V shows the x and y position of the Sun center and the x and y positions of the occulter center during the mission.

7.4. Summary results

Although there has been some slight movement of the occulter and Sun centers with respect to the CCD, these values have been fairly stable. A significant transient occurred during the SOHO interruption in 1998. Apart from occasional intentional spacecraft rolls, the SOHO roll angle with respect to solar north has remained between -0.2° and -0.3°. Corrections to image times were required and their magnitude has varied during the mission. Table V summarizes the status of these values. The corrected roll angle appears in the image header but is not applied to the Level-1 image.

8. Exposure Time Correction

During the early part of the SOHO mission, errors in the reported exposure times were noticed. Although this was a small error, this problem manifested itself as

flashes or flickering in movies of C3 (and C2) images. This effect was most pronounced in movies of running difference images. In this type of movie, each frame is generated by subtracting the preceding image from the present image so that small differences in the exposure time produced noticeable effects. Difference movies were used, in part, to determine the effectiveness of the calculated correction factors. In this section, the methods used to correct this error are presented.

8.1. Sources and evidence of exposure time variation

LASCO exposure times are determined by the main processor which sends a command through a second processor to a third processor that actually opens and closes the shutter. This was different than the original design concept, which was to have the processor that moved the mechanism also determine the exposure time delay. This concept had to be scaled back with the result that there is an uncertainty in the time it takes to send and process the open and close signals that determine the exposure time. The main processor calculates the exposure time from the time it sends out the command to open the shutter and the time it receives the response from the second processor indicating the shutter has been closed.

As a result of the above errors, the reported exposure times were off by 0.2% or more. Two different methods for generating exposure time correction factors were developed in tandem, one by NRL and the other by LAS. The differences between the two methods were very small (10^{-3} to 10^{-4}) and both are generally effective at improving the frame-to-frame variation to better than 0.1%. Both methods assume that the large scale corona changes very slowly on time scales on the order of hours. The method that is used to perform the correction is described below. The correction factor generated by these methods is generally 1.000 ± 0.003 or better indicating this correction to be relatively small. The LAS method is discussed elsewhere (Llebaria and Thernisien, 2001).

8.2. Exposure time correction method

The NRL exposure time correction method computes correction factors for full-field images by comparing the intensities in a select set of regions in the image with the intensities in these same regions in a reference image. In order to decrease the computation time, a smaller array was generated for every image where each element of this smaller array is the median intensity in a 32×32 block of pixels in the original image. Each of these 32×32 blocks is referred to as a super-pixel and this procedure reduces each 1024×1024 pixel image to a 32×32 super-pixel image. In the next step, the intensity in a set of super-pixels in each reduced-size image is ratio'ed to the intensity in the same set of super-pixels in the reduced-size reference image. The sets of super-pixels used for comparison are grouped into 16 regions for C3 and each region contains 10 super-pixels. These regions are shown in

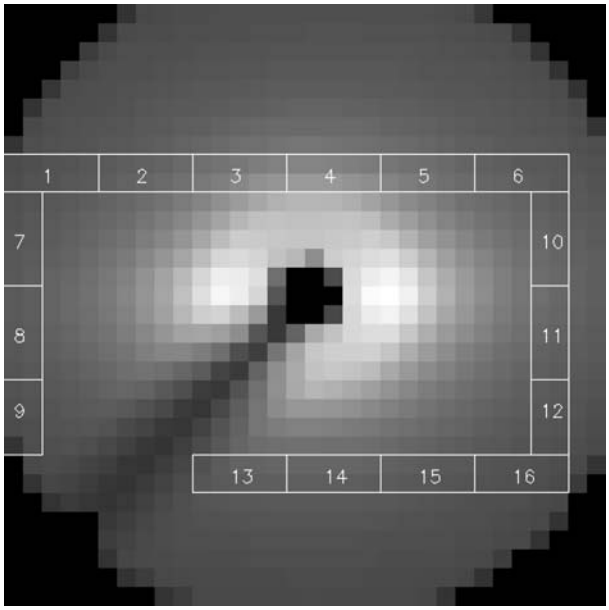

Figure 16. C3 reference image with super-pixel regions indicated.

Figure 16 and were chosen to be within the "equatorial" C3 images collected during 1996. The "equatorial" images are a set of reduced size C3 images which allow higher cadence that were collected during the early part of the mission prior to the implementation of the wavelet compression routine. Each image is compared to the reference image by determining the average of the intensity ratio for each region of super-pixels and this step is repeated for each image in a specified time period, generally 2 weeks. The time history of each region is then examined over this time period.

To distinguish the normal coronal variations in each region from the exposure time fluctuations a two step smoothing process is employed. First, an 11-point median filter is applied to the image ratios of a given region. Next, a 2nd degree polynomial is fit to the nine ratios on either side of the image time desired. Time is used as the independent variable in the polynomial curve fit. No correction for any irregular spacing in the image times is made.

The exposure time correction factor is the observed ratio divided by the smoothed ratio. The final correction factor is the average of the values from all 16 regions. Some non-standard images were also evaluated. All sub-field images, plus the full-field images that could not be corrected by the main routine, are passed to another routine for interpolation and/or extrapolation.

To derive correction factors for sub-field images, only full-field images for which the main routine has already calculated valid exposure factors are used as nearby reference images. Images earlier and later in time than the input image are tested

to see if they have super-pixel blocks that overlap the input image. Two images closest in time to the input image are selected and ratios of overlap of each image to the input image are calculated and averaged. Then a simple linear interpolation between the two times is performed to determine the exposure factor for the input image. A flow chart for the NRL method is shown in Figures 17 and 18.

The time correction procedure is very dependent on the offset bias used to initially correct the images prior to determination of the exposure time correction factors. When working with unprocessed LASCO C3 (and C2) images, care must be taken to use the correct combination of offset bias and correction factor. Because periodic reviews of the CCD bias (discussed above) can lead to changes in the bias values used in image processing no changes are made to existing bias values. This avoids the need to recalculate exposure time correction factors.

As mentioned, the need for this correction can best be seen in difference images. Figure 19 shows a synoptic plot of the running difference images of the corona at ∼18 solar radii. Figure 19a shows the effect of the uncorrected exposure times. Figures 19b and c show the results of the NRl and LAS exposure time correction methods, respectively.

8.3. Summary of exposure time correction results

The uncertainty of the exposure time for each LASCO C3 (and C2) image reported by the LASCO electronics results in a flicker in movies of these images and requires the determination of a slight correction factor. This correction is generally very small ($\sim 1\text{–}3 \times 10^{-3}$) and the two methods developed to correct this problem use the slow variation of the coronal background to derive the correction factor. Both methods are very sensitive to the CCD bias value used for each image and yield very similar results. These factors have been applied to the Level-1 processed images discussed in Section 11.

9. Stray Light

Stray light levels for C3 are based on system tests at NRL and in-flight measurements. The large field-of-view of C3 (16° total) and low stray level makes these measurements extremely difficult in the laboratory. The results show C3 to have an order of magnitude better performance than the levels originally suggested (Brueckner *et al.*, 1995). When comparing C3 stray light levels with the average equatorial coronal brightness at any radial distance, it must be remembered that this telescope is increasingly vignetted toward the inner field limits, and so the CCD detector would be illuminated by the vignetted brightness level rather than the full coronal brightness level. Also, a portion of the stray light, primarily near the occulter, remains in the image and is removed once a background image is subtracted.

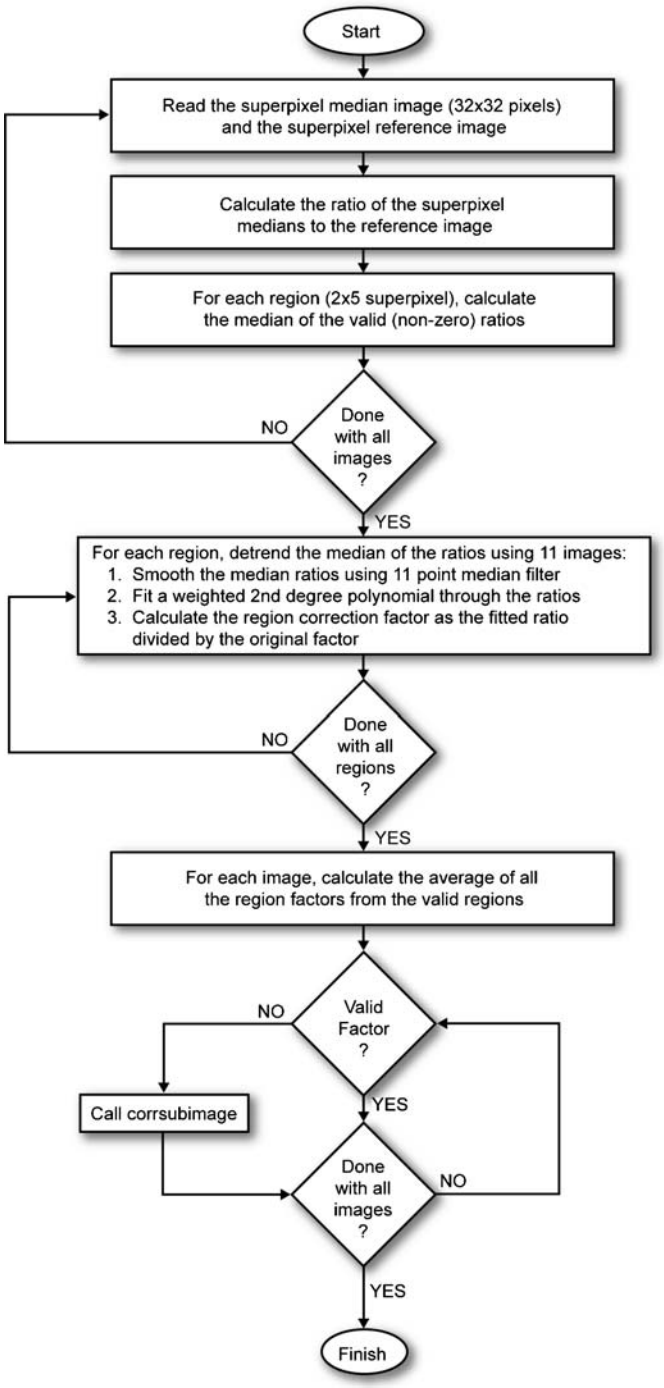

Figure 17. Flow chart for NRLs method of determining exposure time correction factors.

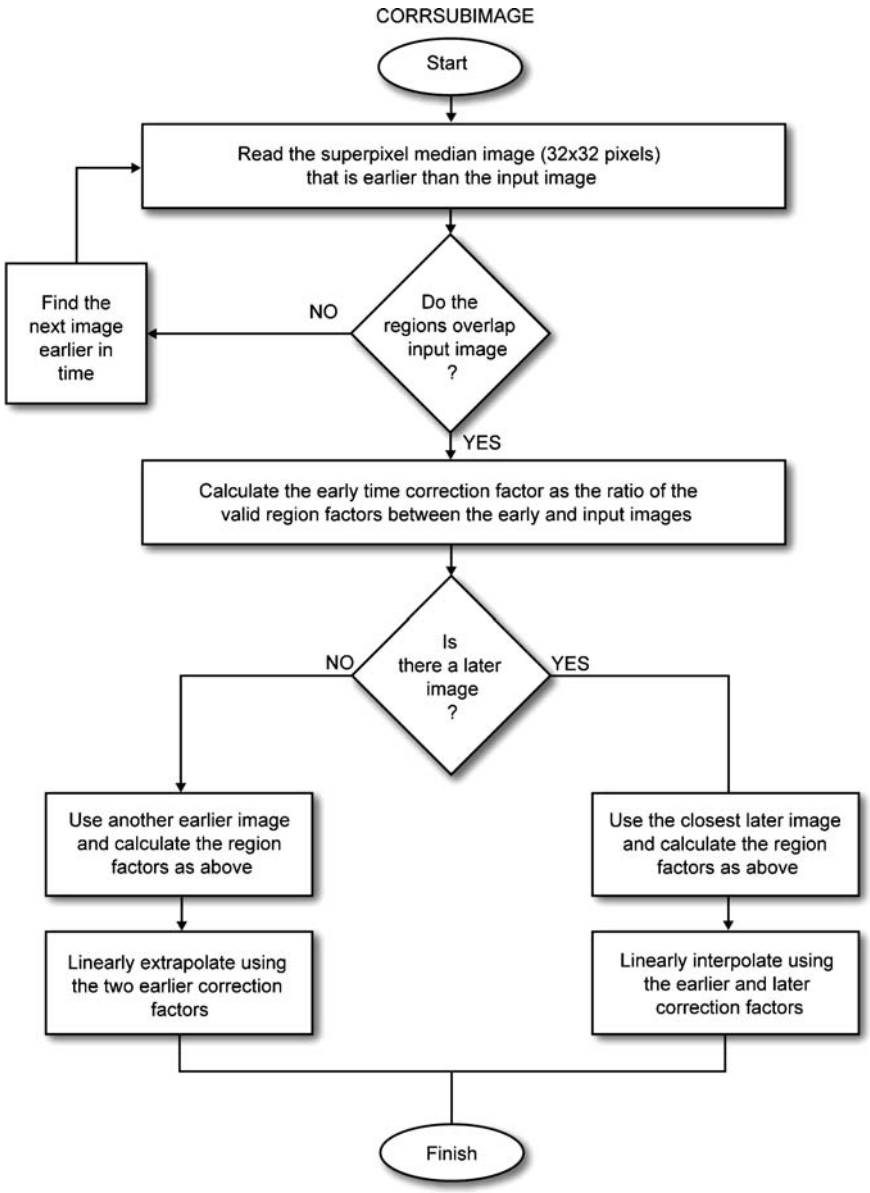

Figure 18. Flow chart for NRLs method of determining exposure time correction factors for images with subfields (incomplete images).

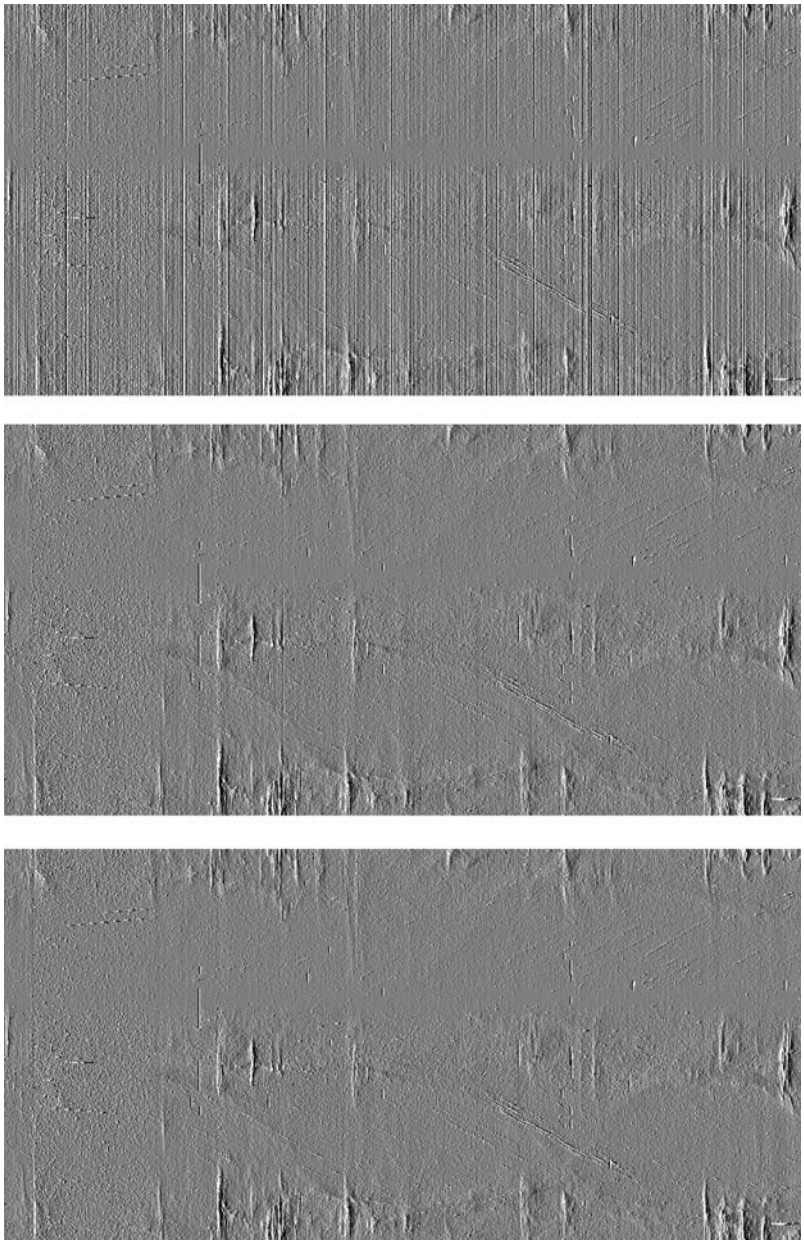

Figure 19. Comparison of NRL and LAS correction methods. See text for discussion of (*top*) original difference map, (*center*) NRL corrected difference map, and (*bottom*) LAS corrected difference map.

9.1. Pre-flight measurements and preliminary results

The C3 stray light test was conducted in the solar instrument test facility on the vacuum tank beam line at NRL in July of 1993. The coronagraph was directly illuminated with a bright quasi-collimated beam of radiation simulating the solar input and a stray light pattern was subsequently recorded with the flight CCD camera. The essential tank optical geometry is shown in Figure 7. For the stray light testing, the calibration light source and color correction filters were replaced with a 2000 W Xenon arc solar simulator. The calibration opals and associated filter wheel were removed.

An additional color filter was used to suppress the infrared and UV portions of the Xenon arc spectrum. A defocused image of the arc plasma was projected onto the collimator telescope aperture stop. A stop placed at the end of the tank (11 m from the C3 aperture) subtended the size of the Sun as seen from the edge of the external occulter. The achromat lens re-imaged this aperture stop onto the front of the coronagraph. The irradiance at the coronagraph A0 aperture was 15% of the solar constant.

This irradiance was measured with a spot photometer in combination with a Macbeth plaque standard diffuser. Redundant measurements with a spectral radiometer confirmed these results. Throughout the testing, the C3 coronagraph directly viewed the back of the tank 11 m away and an intermediate baffle placed $\sim$3 m from the instrument. The measured stray light was $<10^{-12}\ B/B_{\mathrm{Sun}}$. The ultimate stray light level could only be measured for a restricted portion of the field of view because of the very bright return from the heat rejection mirror directly illuminating the baffles in the instrument field of view. The laboratory stray light measurement is consistent with the on-orbit performance.

9.2. In-flight evaluations of stray light

Two primary components of the C3 stray light have been identified in the C3 coronal images and these will be discussed in the following sections. They are (i) a non-radially symmetric ramp that lies diagonally across the C3 field-of-view, and (ii) a constant level that is estimated to be $<1.0 \times 10^{-12}\ B/B_{\mathrm{Sun}}$. A very weak pattern of arcs was also observed in difference images. This pattern is so weak in the outer portions of the FOV that no correction for it was applied to the Level-1 images. However, these features are removed once a background image (Section 10) is subtracted.

9.2.1. *Stray Light Ramp*

Long-term plots of the radial brightness profile above the north and south pole show an annual variation in which the southern plot is about 6 months out of phase with the northern plot. At heights closer to the Sun, the plots overlap. However, further

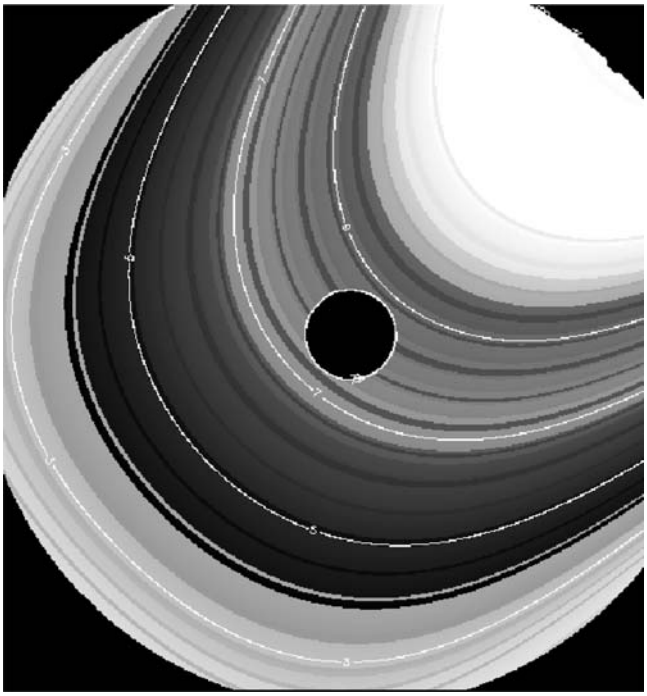

Figure 20. The model of the stray light ramp in C3. Contours are labeled in DN s^{-1} (1 DN s^{-1} = 5.03×10^{-13} B_{Sun}).

from the Sun (e.g., 20 R_{Sun}), the intensities in the north are consistently higher than those in the south. Similarly the intensities at 20 R_{Sun} on the west limb are consistently higher than those in the east.

A detailed discussion of the analysis is presented in Vourlidas and Howard (private communication) but a brief review of the method and results is presented here. The SOHO spacecraft performed a roll maneuver on March 19, 1996. Vourlidas and Howard (private communication) used the images taken at 0 and 180 roll positions.The rolled images were rotated and subtracted from each of the normal images and the median of the six difference images was used for the analysis. This subtraction removed the coronal scene leaving instrumentally generated stray light patterns. The resulting pattern was a ramp and is shown in Figure 20.

Although the source of the stray light was not identified, likely source is a reflection from the CCD surface. Regardless of the source we have established the following characteristics for the stray light:

(1) The stray light over the image is not vignetted. This implies that the source of the light must be after the internal occulter.
(2) The level of stray light depends linearly upon the exposure time (i.e., constant DN s^{-1}).

(3) The shutter is very effective in blocking the direct illumination.
(4) The stray light pattern in the blue filter with much longer exposure times is the same as in the clear filter. This implies that the reflection must be occurring after the filter wheel and is not a reflection of the primary beam off the filter.
(5) The stray light "ramp" is a very low light level effect. The pixel values are between 1 and 13 DN s^{-1} or ISL $<6.5 \times 10^{-12}$ B_{Sun}.
(6) The stray light "ramp" can account for the East-West asymmetry and the North-South asymmetry.
(7) The residual stray light after correction for the ramp are ~2–4 DN/s (1–2 $\times$ 10^{-12} B_{Sun}) which are of the same order as the noise in individual images.

These facts are consistent with a reflection from the CCD surface.

9.2.2. *Constant Stray Light Background*

The technique to obtain the asymmetric stray light pattern cannot determine the symmetric part. In the past this component has been determined by matching the radial gradient of the brightness curve with previous measurements of the corona (Bohlin, Koomen, and Tousey, 1971). This stray light component arises from diffracted light striking the first objective, which creates scattering within the lens. This scattering adds a uniform pall of stray light over the entire field of view.

To determine the constant stray-light background in C3, we have matched the observed radial profiles to those of the F-corona determined by the Zodiacal Light Photometer on the Helios mission. The Helios observations have been summarized by (Leinert, 1981), who modeled the radial brightness of the F-corona a power law of the form $I = kr^{(-\alpha)}$. Radial brightness distributions of the combined C2 (4.5–6.4 R_{Sun}) and C3 (6–28 R_{Sun}) data were fit to a similar functional form. Each position angle was fit separately to account for the eccentricity of the F-corona. An arbitrary level was subtracted from the LASCO observations and then differenced from the Helios F-corona. This arbitrary level was then varied and the one that resulted in the minimum difference at 25 R_{sun} was established as the uniform stray light pall. The level was 6.6×10^{-12} B/B_{Sun}.

9.3. SUMMARY OF STRAY LIGHT RESULTS

In-flight measurements and subsequent analysis have shown the presence of two primary components of stray light, a ramp and a constant background level (~$6.6 \times$ 10^{-12} B_{Sun}). Correction for these two stray light components are applied during the Level-1 processing. No correction is done for a weak background pattern as it has no significant impact on the observed signal and is removed with the subtraction of a background image (Section 10).

10. Background Images

The dominant component of the observed corona is the F (dust) corona. In order to observe the details and changes in the K (electron) corona, we found it quite useful to use the un-calibrated images and to remove the F-corona and stray light by deriving an empirical background model that would be used to reveal the K-corona. This method first generated a daily median image by finding for each pixel the median value for all images on that date. Then the minimum of all daily images for 2 weeks (14 days) on either side of the desired date was computed giving the background image for that date. This computation was performed every week for which data in the 4 week period existed. To obtain the background image for a given date, the background images just prior to and after the desired date were used in a linear interpolation to the desired date. These un-calibrated background images were calibrated to Level-1, using the same procedures and data files as for the direct images and are available to the community. Of course the stray light has been removed from these calibrated background images whereas it is not removed in the un-calibrated images.

It should be noted that these background images may still have a residual K-coronal contribution to them. A background K-signal or a persistent streamer that is present for more than 27 days will not be removed by this simple procedure. For example during the solar minimum period, the equatorial streamer was persistent for many rotations. Such structures can generate artifacts in an image that has had the background image applied and caution should be taken before using them.

11. The Level-1 Data Processing

The application of the above calibrations is included in the Level-1 process. At present only the color filter images have been processed. Processing of the polarization data will be discussed in a separate paper.

11.1. Derivation of the C3 level-1 images

The following list of steps is involved in the processing of the C3 observations to Level-1:

(1) Subtract bias
(2) Divide by exposure time. For Clear filter images these are corrected exposure times.
(3) Replace missing blocks (see Section 11.2).
(4) Apply a calibration factor. For Clear filter images these are the time varying factors.

(5) Apply vignetting function correction.
(6) Subtract stray light
(7) Corrections for geometric distortion.
(8) Multiply by distortion corrected mask containing the occulter, the pylon, and the outer edge. This mask includes missing blocks in certain cases (see Section 11.2).

Figure 1 shows an example of a fully processed image with a background image subtracted.

11.2. Replacing missing blocks

Step 3 (above) of the Level 1 processing of LASCO C3 images involves extrapolation of missing blocks using a method known as "fuzzy logic." This is done to minimize edge effects from the distortion correction, and to eliminate zeros in the middle of the image, which may cause difficulties in analysis. The details of the fuzzy logic algorithm are discussed elsewhere (Lee, Zhang, and Leon-Garcia, 1995). The method works best when the gradient in the vicinity of the missing block boundary is small. There can be considerable extrapolation artifacts when missing blocks are near bright point sources like cosmic rays or stars, near the occulter, or near the edge of the FOV. Before extrapolation, a background image is subtracted from the unprocessed image to minimize the gradient due to the F-corona, and all missing pixels are forced to zero. If there are fewer than 100 blocks missing in an image, the fuzzy logic extrapolation is applied and then the missing blocks in the original image are replaced with the extrapolation plus the fixed background. All missing blocks that have been replaced with extrapolated data are denoted in the image header. The missing blocks are removed from the final image if one of the following is true: (i) 16 or more blocks in a zone are missing, where a zone is defined as contiguous missing blocks plus 1 block buffer adjacent to missing blocks or (ii) any missing block is adjacent to the edge of image.

12. Conclusions

In this paper were have presented a comprehensive review of the LASCO C3 calibration. The paper is organized so that each section can be read in isolation with summary information included at the end of each section. For the most part this calibration has been in place since launch. During the course of the SOHO mission further information, much of it derived from star observations, has allowed us to refine the details of this calibration so that corrections to the photometric calibrations, the vignetting function, geometric distortion effects, stray light, and exposure and observation times have all been optimized. Using these recent refinements we have generated a Level-1 data set so that a majority of the C3 data set is available

without need of further correction. I Information on this data set is located on the LASCO web site (*http://lasco-www.nrl.navy.mil/*).

Acknowledgements

This work was supported by NASA and the Office of Naval Research. The SOHO/LASCO data used here are produced by a consortium of the Naval Research Laboratory (USA), Max-Planck-Institut für Aeronomie (Germany), Laboratoire d'Astronomie Spatiale (France), and the University of Birmingham (UK). SOHO is a project of international cooperation between ESA and NASA.

References

Bohlin, J. D., Koomen, M. J., and Tousey, R.: 1971, *Solar Phys.* **21**, 408.
Brueckner, G. E., Howard, R. A., Koomen, M. J., Korendyke, C. M., Michels, D. J., Moses, J. D., *et al.*: 1995, *Solar Phys.* **162**, 357.
Evans, J. W.: 1948, *J. Opt. Soc. Am.* **38**, 1083
Gray, D. F.: 1992, *The Observation and Analysis of Stellar Photospheres*, Cambridge University Press, New York, p94.
Hardie, R. H.: 1962, in W. A. Hiltner (ed.), *Astrophysical Techniques, Stars and Stellar Systems*, Vol. II, University of Chicago Press, Chicago, 178.
Janesick, J. R.: 2001, *Scientific Charge-Coupled Devices*, SPIE Press, Bellingham, Washington.
Johnson, H. L.: 1980, *Rev. Mex. Astron. Astrof.* **5**, 25.
Johnson, H. L. and Mitchell, R. I.: 1975, *Rev. Mex. Astron. Astrof.* **1**, 299.
Johnson, H. L. and Mitchell, R. I.: 1977, *Rev. Mex. Astron. Astrof.* **2**, 269.
Koomen, M.J., Detwiler, C.R., Brueckner, G.E., Coopper, H.W., and Tousey, R.: 1975, *Appl. Opt.* **14**, 743.
Lee, X., Zhang, Y.-Q., and Leon-Garcia, A.: 1995, *IEEE Trans. Imag. Proc.* **4**, 3.
Llebaria, A. and Thernisien, A.: 2001, in J.-L. Starck and F.D. Murtagh (eds.), *Astronomical Data Analysis, Proc. SPIE* **4477**, 265.
Lyot, B.: 1930, *Comptes Rendus Acad. Sci. Paris* **191**, 834.
Leinert, C., Richter, I., Pitz, E., and Planck, B.: 1981, *Astron. Astrophys.* **103**, 177.
Mallama, A., Wang, D., and Howard, R. A.: 2002, *Icarus* **155**, 253.
MacQueen, R. M., Gosling, J. T., Hildner, E., Munro, R. H., Poland, A. I., and Ross, C. L.: 1974, *Soc. Photo-Opt. Instrum. Eng.* **44**, 207
MacQueen, R. M., Csoeke-Poeckh, A., Hildner, E., House, L., Reynolds, R., Stranger, A., *et al.*: 1980, *Solar Phys.* **65**, 91.
Moran, T. G., Davila, J. M., Morrill, J. S., Wang, D., and Howard, R. A.: in Press, *Solar Phys.*
Newkirk, G. and Bohlin, J. D.: 1963, *Appl. Opt.* **2**, 131.
Purcell, J. D. and Koomen, M. J.: 1962, Report of NRL Progress, September Issue.
Smith, W. J.: 2000, *Modern Optical Engineering*, 3rd edn., McGraw Hill, New York, 143.
Thernisien, A. F., Morrill, J. S., Howard, R. A., and Wang, D.: in press, *Solar Phys.*
Tousey, R.: 1965, *Ann. Astrophys.* **28**, 600.
White, R. L. and Percival, J. W.: 1994, in L. M. Stepp (ed.), *Advanced Technology Optical Telescopes V., Proc. SPIE* **2194**, 703.